The MoN–TaN system: Role of vacancies in phase stability and mechanical properties

F.F. Klimashin [a], L. Lobmaier [a], N. Koutná [a], D. Holec [b], P.H. Mayrhofer [a,*]

[a] Institute of Materials Science and Technology, TU Wien, 1060 Vienna, Austria
[b] Department of Materials Science, Montanuniversität Leoben, 8700 Leoben, Austria

HIGHLIGHTS

- Experimental and first principle insights into the barely explored MoN–TaN.
- Magnetron sputtered MoN–TaN films with a wide composition range.
- Role of vacancies in favouring the cubic structure over other polymorphs.
- 140% toughness enhancement through cubic-structured $Mo_{1-x}Ta_xN_y$ solid solutions realised by nitrogen vacancies.

GRAPHICAL ABSTRACT
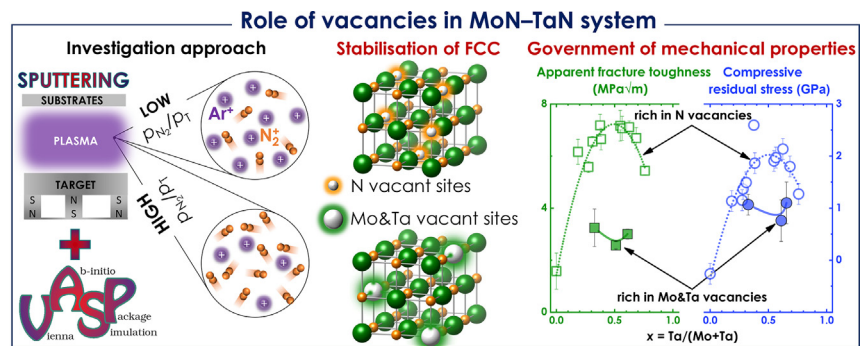
ARTICLE INFO

ABSTRACT

Face-centred cubic (fcc-) Mo–N and Ta–N exhibit an inherent driving force for vacancy formation. To study their interaction and effects on structural evolution and mechanical properties, we synthesised Mo–Ta–N coatings by reactive magnetron sputtering using nitrogen-to-total pressure ratios, p_{N2}/p_T, of 0.32 and 0.69.

Low p_{N2}/p_T results in high concentration of N vacancies, which stabilise single-phase fcc-$Mo_{1-x}Ta_xN_y$ up to $x = 0.76$. These solid solutions follow the $MoN_{0.5}$–$Ta_{0.875}N_{0.875}$ quasi-binary tie line. Compressive residual stresses, σ, indentation hardness, H, and toughness, K_C, increase with Ta content, reaching their maxima of (on average) -2.0 GPa, 28 GPa, and 7.0 MPa√m, respectively, within the x range 0.38–0.69. Higher Ta contents favour higher concentration of metal vacancies deteriorating the properties.

High p_{N2}/p_T favours the formation of fcc-$Mo_{1-x}Ta_xN_y$ rich in metal vacancies, which however always coexists with a hexagonal phase. Within the x range 0.33–0.66, the fraction of the hexagonal phase is negligible, and σ, H, and K_C deviate from -1.0 GPa, 28 GPa, and 2.9 MPa√m, respectively, within the error of measurements.

The combination of experimental and theoretical studies demonstrates the power of point defects in stabilising desired crystal structures and improving mechanical properties through the thereby tuned atomic configuration.

1. Introduction

Physical vapour deposition (PVD) techniques in combination with low substrate temperatures allow for the generation of various metastable, supersaturated, and even thermodynamically unstable structures with a high defect density. In particular vacancies – present in nearly any PVD processed materials (even to a very large extent) – significantly influence structure and properties. Quantification of these important defects is anything but a trivial experimental issue [1]. However, the combination of computational and experimental materials science is an excellent tool for understanding the impact of vacancies on the formation and properties of (non-stoichiometric) transition-metal nitrides [2–5], borides [6–8], carbides [9–12], oxides [13–15] or mixtures thereof

* Corresponding author.
  E-mail address: paul.mayrhofer@tuwien.ac.at (P.H. Mayrhofer).

[16–18]. Motivated by the inherent driving force of the cubic phases within binary Mo–N and Ta–N for nitrogen and metal vacancies [19–21], we developed and investigated cubic-phase materials within the hitherto barely investgated ternary system Mo–Ta–N with different concentration of vacant sites on the nitrogen and metal sublattices. Of particular interest are mechanical properties of these materials as both consituting nitrides are predicted to enhance the toughness of the transition-metal nitride alloys [22].

2. Methods

2.1. Experimental

The binary Mo–N and Ta–N as well as ternary Mo–Ta–N coatings were synthesised in mixed Ar and N_2 DC glow discharges (both gases with purity above 99.999%) in a modified Leybold Heraeus Z400 magnetron sputtering system. Mo-rich quasi-binary nitride coatings were synthesised from a molybdenum target (99.97% purity, Ø75 mm) by placing various amounts of small Ta disks (99.95% purity, Ø6 x 3 mm) on the race track. Correspondingly, the Ta-rich compositions were obtained by using a tantalum target (99.95% purity, Ø75 mm), where various amounts of small Mo disks (99.97% purity, Ø5 x 3 mm) were uniformly placed on the race track. All depositions were prepared at a constant target current of 0.4 A, floating potential at the substrates (~ -15 V), and a constant substrate temperature of 450 ± 20 °C. Prior to every deposition processes, the chamber was evacuated to a base pressure of $p_{base} ≤ 5·10^{−4}$ Pa. The depositions were prepared with two different nitrogen-to-total pressure ratios, p_{N2}/p_T, of 0.32 and 0.69 and at a total pressure, p_T, of 0.35 Pa. Single-crystal silicon, Si (100), and polycrystalline austenite steel substrates were ultrasonically precleaned in acetone and alcohol (for 5 min) before loading to the deposition chamber, and r.f. plasma etched (within the chamber) prior to the deposition using an argon pressure of 2 Pa, a voltage of 350 V, and a pulse frequency of 50 kHz and a width of 2656 ns. Before venting the deposition chamber, the substrates were cooled down to a temperature below 100 °C, in order to minimise surface chemistry alterations [23].

X-ray diffraction was performed in symmetric (Bragg-Brentano) and asymmetric (glancing angle, with 2° incidence angle) geometries using monochromised Cu $K_α$ radiation ($λ$ = 1.54 Å). The stress-free lattice parameters of the single-phase coatings, a_0, and dimensions of the coherently scattering domains (CSD) were obtained using the $sin^2ψ$ method [24] and Williamson-Hall plot, respectively. A Poisson's ratio of 0.35 – which is virtually insensitive to the metal fraction Ta/(Mo + Ta) – was chosen based on the computational results of Koutná et al. [25]. The scanning electron microscopy (SEM) morphological investigations were performed using the Schottky emitter that results in the spatial resolution of ~2 nm. Energy dispersive X-ray spectroscopy (EDX), calibrated using SECS Light-element Calibration Standard CrN (Ardennes Analytique SPRL), was used for chemical investigations of the coatings.

The nanoindentation measurements were carried out using an ultra-micro-indentation system (UMIS) equipped with a Berkovich diamond tip in the load range of 3–45 mN. To guarantee the accuracy of the measurements, the instrument was calibrated using a fused silica standard (E = 72.5 GPa [26]) and a few other reference samples as shown in Ref. [27]. The evaluation of the coating-only indentation hardness, H, and modulus, E, is described in detail in Refs. [28, 29, 30]. The fracture toughness, K_C, was obtained by the nanoindentation cracking technique [31–34], using a cube-corner indenter, in accord with the formula devised by Lawn, Evans, and Marshall (LEM):

$$K_C = α·\sqrt{\frac{E}{H}} \frac{P}{c^{3/2}} \tag{1}$$

where c is the average length of the cracks emanating from the corners of an indentation imprint after applying a load P and obtained by imaging the indentations via SEM and $α$ is an empirical calibration constant.

In this study, $α$ is taken for 0.036 according to the study of Harding, Pharr, and Oliver [35], which considers a wider range of brittle materials than their earlier work reporting on $α$ of 0.0319 [36]. If nanoindentation data on soda-lime glass in study of Harding et al. are not considered, $α$ will become 0.040, as shown by Pharr [37]. Additionally, a value of 0.0535 is obtained by Scharf et al. for hard SiC-N coatings [38]. Both latter values would evidently provide nearly 11% and 50% higher K_C than in the present study (for numbers see Table 1 in Supplementary Material). Hence, our results represent rather the lower limit of K_C according to the LEM model. To guarantee the measurement accuracy, five indents were made at every load within the range 50–300 mN in 50 mN steps. The use of a cube-corner indenter allows to substantially reduce the cracking threshold and hence to measure fracture toughness of thin coatings [36,37]. Note that due to the presence of residual stresses in the coatings, K_C characterises the fracture behaviour of the system coating/substrate, in other words K_C quantifies the *apparent* fracture toughness [39], which is highly useful for both fundamental [40] and applied [41] aspects. The residual stresses, $σ$, were calculated using the Stoney Eq. [42–44], after measuring the curvature of the coated Si (100) substrates by means of a chromatographic, confocal profilometer Nanovea PS50. To analyse the impact of $σ$ on K_C, the stress intensity factor, K, was calculated accoring to the following equation (taking the geometry term $Ω$ for 0.3 [45]):

$$K = σ·\sqrt{πΩc} \tag{2}$$

2.2. Computational

Density Functional Theory (DFT) calculations were carried out employing the Vienna Ab-initio Simulation Package (VASP) [46,47] together with the projector augmented plane wave (PAW) pseudopotentials. Exchange and correlation effects were treated using the Perdew-Burke-Ernzerhof (PBE) generalised gradient approximation (GGA) [48]. The plane-wave cut-off energy was set to 700 eV and the k-vector sampling of the Brillouin zone was checked to provide a total energy accuracy of about $10^{−3}$ eV/at. According to our experimental results, models for $Mo_{1-x}Ta_xN$ solid solutions were based on the cubic NaCl (*Fm-3 m*, #225), and the hexagonal NiAs (*P6_3/mmc*, #194) and WC (*P-6 m2*, #187) type structures. Various vacancy types (Mo, Ta, or N) and concentrations, as well as the chemical disorder on the metal sublattice were generated according to the Special Quasi-random Structure (SQS) method [49], and compared in terms of formation energies obtained by the following equation:

$$E_f = \left(E_T − \sum_i n_i·μ_i \right) / \sum_i n_i \tag{3}$$

where E_T is the total energy, n_i and $μ_i$ are the number and chemical potential of the i atom species Mo, Ta, and N atoms. To investigate the impact of vacancies on phase formation within the system Mo–Ta–N, four tie lines preserving their stoichiometries were chosen based on our computational pre-studies [20]. Three of them are based on the low-energy binary defected structures. These are $Ta_{0.75}N$, $MoN_{0.5}$, and $Ta_{0.875}N_{0.875}$ (12.5% Schottky defects) and they result in the tie lines $Mo_{0.75}N–Ta_{0.75}N$, $MoN_{0.5}–TaN_{0.5}$, and $Mo_{0.875}N_{0.875}–Ta_{0.875}N_{0.875}$. The fourth tie line MoN–TaN reflects the formation of the defect-free structures. For a more convenient comparison of the formation energies of the different structures, a parabolic fit of the calculated data points for the defect-free structures, i.e. those following the MoN–TaN quasi-binary tie line, was subtracted from parabolic fits for all other investigated structures. By investigating the impact of vacancies on the stability of the cubic, NaCl-type structures with respect to the hexagonal, NiAs- and WC-type structures, the chemical potentials have been set to that of bulk bcc-structured Mo, $μ_{Mo}$(bcc–Mo), and Ta, $μ_{Ta}$(bcc–
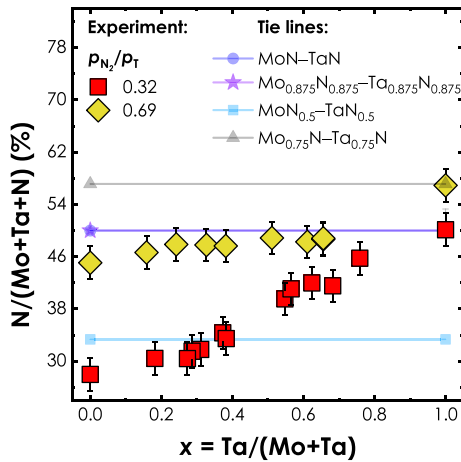
Fig. 1. The normalised nitrogen concentration of our Mo–Ta–N coatings as a function of their Ta/(Mo + Ta) ratio obtained by EDS. The quasi-binary tie lines, with constant N or Me content over the entire Ta range $0 \leq x \leq 1$, are based on the low-energy configuration of one of the boundary system ($MoN_{0.5}$, $Ta_{0.875}N_{0.875}$, and $Ta_{0.75}N$) [20].

Ta), as well as of N_2 molecule, $\mu_N(N_2)$. While $\mu_N - \mu_N(N_2) = 0$ indicates N-rich conditions during synthesis [50], that is high p_{N2}/p_T, for modelling of the N-poor conditions, hence low p_{N2}/p_T, the value of the nitrogen chemical potential $\mu_N - \mu_N(N_2)$ was shifted from 0 to -1.5 eV as follows from comparison of y in γ-MoN_y in the current study and our previous calculations [19,20].

3. Results

3.1. Microstructure

The chemical composition of our coatings synthesised at low nitrogen-to-total pressure ratio, $p_{N2}/p_T = 0.32$, suggests a gradual increase of the normalised nitrogen concentration, i.e. N/(Mo + Ta + N) ratio, from 28 to 50 at.% with increasing Ta/(Mo + Ta) ratio from $x = 0$ to 1, see Fig. 1. In contrast, at high nitrogen-to-total pressure ratio, $p_{N2}/p_T = 0.69$, the nitrogen concentration increases from 45 to 48 at.% when increasing the Ta content from $x = 0$ to 0.25, and further from 48 to 50 at.% when increasing the Ta content from 0.25 to 0.7. Especially for the Ta contents between 0.25 and 0.7, the variation in N content is

within the error of measurement. Only binary Ta–N, deposited at $p_{N2}/p_T = 0.69$, shows a much higher N concentration of 57 at.%, Fig. 1.

Thus, the compositions of our Mo–Ta–N coatings are closer to the quasi-binary tie line $MoN_{0.5}$–TaN when prepared with a low nitrogen-to-total pressure ratio ($p_{N2}/p_T = 0.32$) and the quasi-binary tie line MoN–TaN when prepared with a high nitrogen-to-total pressure ratio ($p_{N2}/p_T = 0.69$). From these chemical investigations, of course any Schottky defect concentration would be possible as well, therefore we added to Fig. 1 the $Mo_{0.875}N_{0.875}$–$Ta_{0.875}N_{0.875}$ tie line for example. The chemistry of our coatings prepared with $p_{N2}/p_T = 0.32$ could thus also follow the $MoN_{0.5}$–$Ta_{0.875}N_{0.875}$ tie line.

All prepared coatings reveal a smooth surface and a dense growth morphology, which is a bit more columnar when using a low p_{N2}/p_T ratio, compare Fig. 2a ($p_{N2}/p_T = 0.32$) with 2b ($p_{N2}/p_T = 0.69$). The growth rates of the coatings deposited at $p_{N2}/p_T = 0.32$ are approximately 30% above those deposited at $p_{N2}/p_T = 0.69$ for a similar x, see Fig. 3. Generally, higher Ta contents x result in lower deposition rates due to significantly higher target poisoning effects caused by the more negative enthalpy of a nitride formation (at 298 K), compare -60.10 kcal/mol for TaN or -65.00 kcal/mol for Ta_2N with -9.75 kcal/mol for $MoN_{0.5}$ [51]. Quantitatively expressed, the addition of Ta disks on the Mo-target results in a reduction of deposition rate from 4.3 to 1.2 μm/h (low p_{N2}/p_T) and from 3.0 to 1.2 μm/h (high p_{N2}/p_T) for coatings having $x = 0$ and 1, respectively. This phenomenon provides an explanation for the discrepancies in deposition rates, when sputtering Mo target with Ta disks and Ta target with Mo disks for both p_{N2}/p_T conditions (Fig. 3). Nevertheless, their growth morphologies and N contents are comparable (for similar Ta and Mo content) irrespective of whether a Ta target with Mo disks or a Mo target with Ta disks was used.

The XRD investigations of the coatings deposited with low p_{N2}/p_T of 0.32 reveal the formation of cubic-phase solid solutions with preferred (200) orientation and small coherently scattering domains (CSD) of ~23 ± 8 nm for Ta contents x below 0.76, see the corresponding XRD patterns in Fig. 4a. The Mo-free Ta–N coating exhibits also pronounced XRD peaks from a hexagonal phase.

On the contrary, in ternary coatings prepared with high p_{N2}/p_T of 0.69, a hexagonal phase (NiAs or WC prototype) always develops along with the cubic, see Fig. 4b. Its fraction in the compounds is however insignificant, and the reflections in Fig. 4b become visible only due to a logarithmic scale of the XRD patterns. A possible reason for the dual-phase nature of Mo-rich compounds with a stoichiometry close to 1:1 might originate from elastic and phonon instabilities of
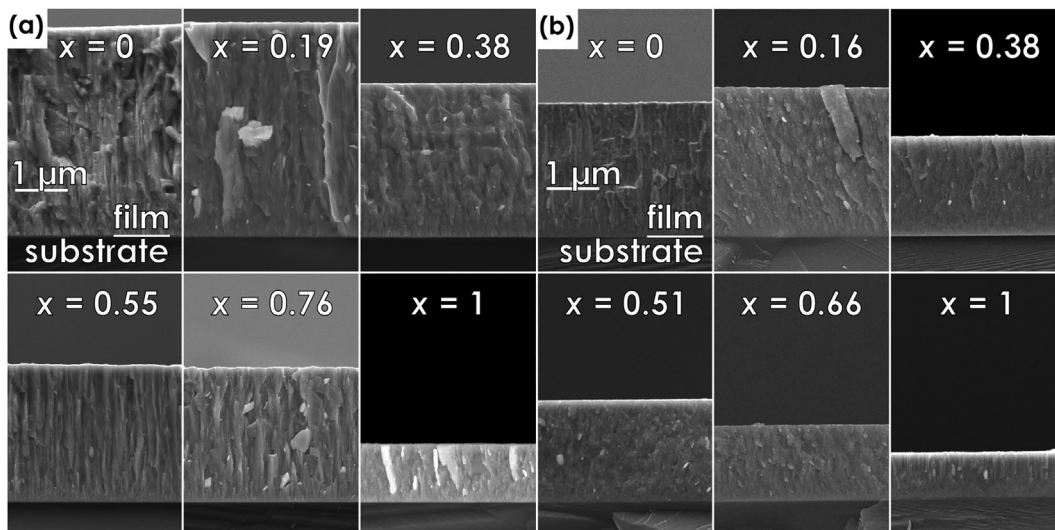

Fig. 2. SEM fracture cross-sections of selected Mo–Ta–N coatings prepared at $p_{N2}/p_T = 0.32$ (a) and 0.69 (b) with x representing their Ta/(Mo + Ta) ratio.
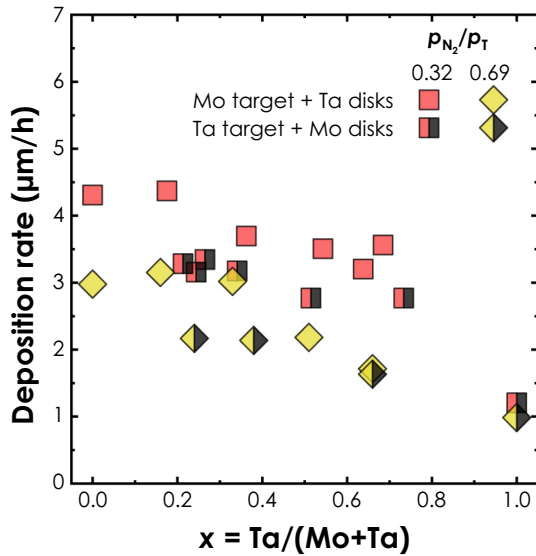
Fig. 3. Growth rates of our Mo–Ta–N coatings deposited with $p_{N2}/p_T = 0.32$ (red-filled and red-black-filled squares) and 0.69 (yellow-filled and yellow-black-filled diamonds) as a function of their Ta/(Mo + Ta) ratio. The single-colour filled symbols refer to the coatings prepared from Mo target with the addition of Ta disks, and the bicolour filled symbols refer to the coatings from Ta targets with the addition of Mo disks.

the strong (200) preferential growth decreases, especially when using a high p_{N2}/p_T ratio, which in further consequence causes a strong reduction of the superstructure reflections. But also the overall N content significantly increases with the Ta content, and ordering of N-sublattice vacancies is not preferred for Ta–N compounds [20].

An essential difference between the two coating series (prepared with low and high p_{N2}/p_T) is that the coatings prepared with a high p_{N2}/p_T of 0.69 exhibit a finer growth morphology (Fig. 2b). This might originate from additional nucleation sites provided by excessive nitrogen and hexagonal phases interrupting the columnar preferential growth. A more frequent re-nucleation of the fcc-$Mo_{1-x}Ta_xN_y$ grains is also reflected in smaller CSD of ~14 ± 5 nm. A schematic illustration of the phase fractions for the coatings prepared with low or high p_{N2}/p_T is summarised in the bicolour plots of Fig. 4c.

The stress-free lattice parameter, a_0, of the understoichiometric binary γ-$MoN_{0.39}$ (prepared with the low p_{N2}/p_T of 0.32) is 0.418 ± 0.003 nm, lying thus between 0.420 nm and 0.416 nm calculated for γ-$MoN_{0.50}$ and γ-$MoN_{0.39}$, respectively [19]. The partially ordered γ'-$MoN_{0.82}$ synthesised with the high p_{N2}/p_T of 0.69 exhibits a_0 of 0.423 ± 0.003 nm, which is significantly below 0.430 nm obtained for a N-vacancy containing fcc-MoN_y of comparable chemical composition [19]. Only if vacancies on both Mo and N sublattices are considered, the ab initio calculated lattice parameter of γ'-$MoN_{0.82}$ matches. The stress-free lattice parameter, a_0, of the cubic-structured $Mo_{1-x}Ta_xN_y$ solid solutions, prepared with low p_{N2}/p_T increases nearly linearly from 0.418 ± 0.003 to 0.435 ± 0.003 nm with increasing Ta content from $x = 0$ to 0.76. The Mo–Ta–N coatings prepared with high p_{N2}/p_T as well as the binary Ta–N (both p_{N2}/p_T conditions) crystallise with a dual-phase structure, thus making the calculation of the stress-free lattice parameter unreliable due to heterogeneity of the elastic constants (corresponding symbols are shown slightly transparent in Fig. 5).

Energy of formation helps to shed light on the structural development of the cubic phases. In particular, a crucial role plays the nitrogen chemical potential, μ_N - $\mu_N(N_2)$, which can be associated with the nitrogen-to-total pressure ratio used during reactive sputtering [50]. The left plot in Fig. 6a represents the data of the individual cubic-structured solid solutions for μ_N - $\mu_N(N_2) = 0$ – which mimics N_2-rich conditions during reactive sputtering – suggesting that the 25% Me-vacant solid solutions (along the $Mo_{0.75}N$–$Ta_{0.75}N$ quasi-binary tie line) win along the entire Ta-range. At the Mo-rich side, the 50% N-vacant as well as the 12.5% Schottky defected structures come close, but at the Ta-rich side only the 12.5% Schottky defected structure
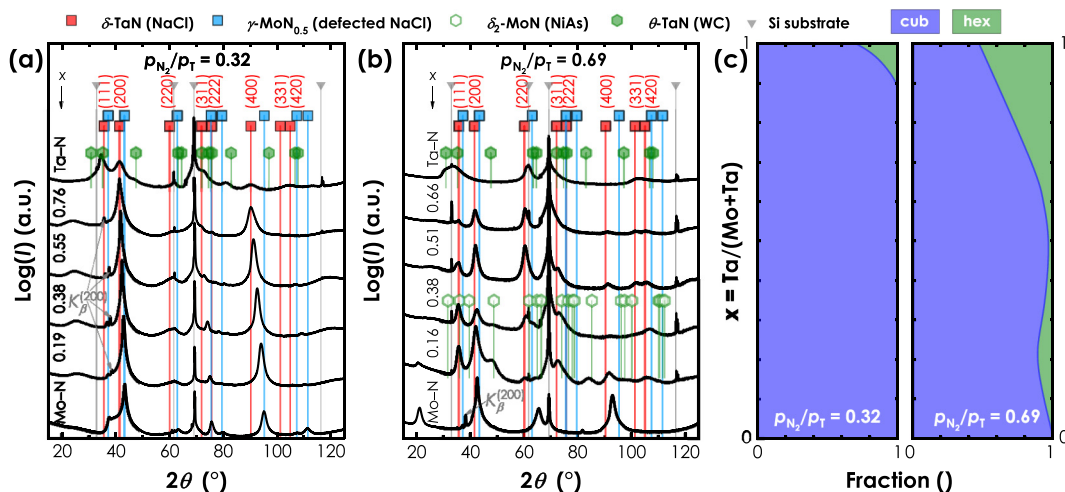
defect-free γ-MoN [52]. Computational study of Bouamama et al. on defect-free face-centred cubic (fcc-) $Mo_{1-x}Ta_xN$ suggest that fcc-$Mo_{1-x}Ta_xN$ can be stabilised for Ta contents $x > 0.27$ [53] (and even less than 0.09 as suggested by the SQS method [25]). Indeed, also for our experiments the fraction of fcc-$Mo_{1-x}Ta_xN_y$ increases with Ta concentration (starting from $x > 0.16$) reaching its maximum for $0.33 < x < 0.66$. The molybdenum nitride itself is composed of an fcc phase, and even exhibits a superstructure, see the superstructure reflections at $2\theta \approx 21°$ in Fig. 4b. These originate from partial ordering of N-sublattice vacancies causing the formation of γ'-$MoN_{0.82}$, as reported in [19]. No superstructure reflections are detectable for understoichiometric γ-$MoN_{0.39}$ (with respect to stoichiometric $MoN_{0.50}$). Also the ternaries with low Ta content exhibit such superstructure reflections (Fig. 4b). With increasing Ta content,

Fig. 4. Logarithmically scaled XRD patterns (symmetric scans) of significant coatings in the system Mo–Ta–N deposited at low p_{N2}/p_T of 0.32 (a) and high p_{N2}/p_T of 0.69 (b) with increasing Ta/(Mo + Ta) ratio, from bottom to top. The indicated phases are δ-TaN (NaCl prototype, ICDD 00–049-1283), γ-$MoN_{0.5}$ (NaCl prototype, ICDD 00–025-1366), θ-TaN (WC prototype, ICDD 04–003-2154), and δ_2-MoN (NiAs prototype, ICDD 04–012-3451). The K_β reflections are due to the highly intense peaks of (200) strongly oriented coatings. The bicolour plots (c) represent a schematic illustration of the phase composition.
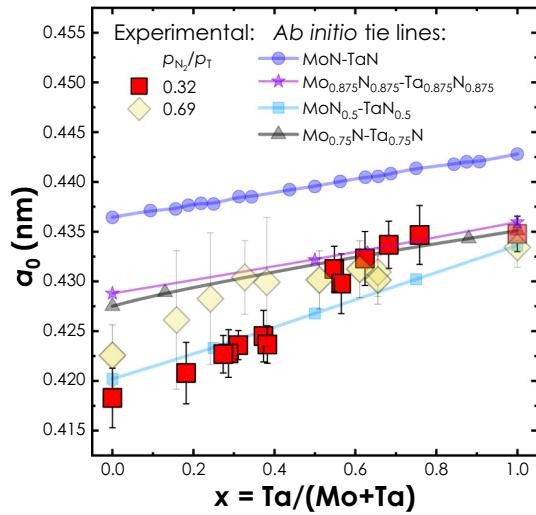
Fig. 5. Stress-free lattice parameters of the cubic-structured solid solutions $Mo_{1-x}Ta_xN_y$ prepared with a low p_{N2}/p_T of 0.32 (red-filled squares) and dual-phase Mo–Ta–N coatings obtained at a high p_{N2}/p_T of 0.69 (yellow-filled diamonds). The latter are shown slightly transparent as the heterogeneity of the elastic constants was not taken into account. The ab initio obtained lattice parameters for fcc-structured solid solutions along the quasi-binary tie lines MoN–TaN, $Mo_{0.875}N_{0.875}$–$Ta_{0.875}N_{0.875}$ (with 12.5% Schottky defects), $MoN_{0.5}$–$TaN_{0.5}$ (50% N vacancies), $Mo_{0.75}N$–$Ta_{0.75}N$ (25% Me vacancies) are indicated by smaller circle, asterisk, cube, and triangle symbols, respectively.

comes close. The right plot in Fig. 6a represents the data of the individual cubic-structured solid solutions for $\mu_N - \mu_N(N_2) = -1.5$ eV – which mimics N_2-poor conditions during sputtering and where the formation of understoichiometric γ-$MoN_{0.38-0.44}$ is favoured [19] – suggesting that the 25% Me-vacant solid solutions lose against the 12.5% Schottky defected or 50% N-vacant solid solutions. The latter win up to $x = 0.85$ and are surpassed by the 12.5% Schottky defected solid solutions for $x > 0.85$. This is in agreement with the general tendency of fcc-MoN to prefer N vacancies and fcc-TaN to prefer Me vacancies or Schottky defects.

Hence, for the solid solutions formed at low p_{N2}/p_T, the compositions along the quasi-binary $MoN_{0.5}$–TaN tie line (which could be possible

when considering only the chemistry of the coatings prepared with low p_{N2}/p_T) are clearly outperformed energetically by the compositions along the quasi-binary $MoN_{0.5}$–$Ta_{0.875}N_{0.875}$ tie line (combining the low-energy configurations along $MoN_{0.5}$–$TaN_{0.5}$ for Mo-rich and $Mo_{0.875}N_{0.875}$–$Ta_{0.875}N_{0.875}$ for Ta-rich compositions). The formation of fcc-$Ta_{0.875}N_{0.875}$ in the dual-phase Ta–N is indeed probable. If $Ta_{0.75}N$ forms, the coexisting hexagonal phase should have a significantly lower N content (N/Ta $<<$ 1, like Ta_2N) to meet the overall chemical composition. This seems to be rather unlikely based on the binary phase diagram showing that these phases are not neighbours. If $Ta_{0.875}N_{0.875}$ forms, the coexisting hexagonal phase should have a N/Ta ratio of about 1, which is reasonable also based on the phase diagram. Interestingly enough, also the stress-free lattice parameter matches the computational values obtained for fcc-$Ta_{0.875}N_{0.875}$ despite heterogeneity of the elastic constants.

In contrast, for the solid solutions formed at high p_{N2}/p_T, structural description of the cubic phase appears more challenging due to lack of supportive data on the stress-free lattice parameter. One of the boundaries, γ'-$MoN_{0.82}$, was found to form with vacancies on both Mo and N sublattices (Schottky defects). Another boundary compound, Ta–N, forms with an N content of ~57 at.%. If $Ta_{0.875}N_{0.875}$ forms, the N/Ta ratio of the coexisting hexagonal phase should be above 1, like TaN_2, while the XRD studies (Fig. 4b) indicate the formation of the WC-type TaN (N/Ta = 1). Consequently, the formation of fcc-$Ta_{0.75}N$ (~25% metal vacancies) is most likely when using a high p_{N2}/p_T of 0.69. Thus, the fcc-Mo–Ta–N phase appears to form with a much higher concentration of vacancies on the metal sublattice.

A comparison of the formation energies further allows to rate the possibility of cubic or hexagonal phase formation. They also reveal why ternary Mo–Ta–N synthesised at low p_{N2}/p_T ratio rather form single-phase solid solutions, while at high p_{N2}/p_T ratio hexagonal and cubic phases form simultaneously. Energetically, hexagonal phases are preferred over defect-free cubic structures within the entire composition range, see Fig. 6b ("no vacancies"). Mo-rich solid solutions favour the NiAs-type for $x < 0.35$, while for higher Ta contents the WC-type structure should develop. The cubic NaCl-type structure is energetically favoured over the hexagonal ones (NiAs and WC types) along the entire Ta composition range if their N sublattice contains 50% vacant N sites (i.e., solid solutions along the quasi-binary $MoN_{0.5}$–$TaN_{0.5}$ tie line). If 12.5% Schottky defects form (i.e., solid solutions along the quasi-binary $Mo_{0.875}N_{0.875}$–$Ta_{0.875}N_{0.875}$ tie line), the cubic NaCl-type

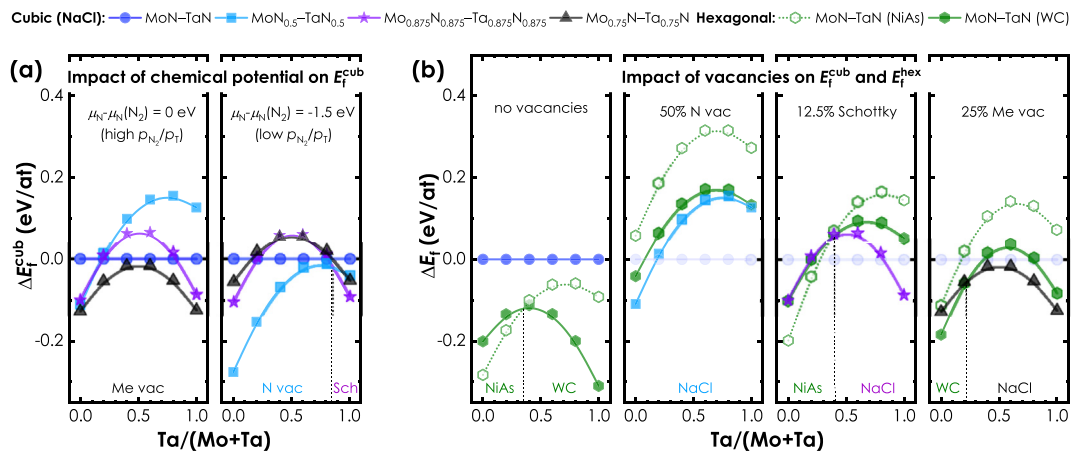**Fig. 6.** (a) Differences in energy of formation between defected and defect-free cubic structures $\Delta E_f^{cub} = E_f^{cub} - E_f^{cub}$(defect-free) shown as circles, cubes, asterisks, and triangles for no vacancies, 50% N vac, 12.5% Schottky, and 25% Me vac, respectively. The chemical potentials μ_{Me} and μ_N are set to that of bulk bcc-structured metals, μ_{Me}(bcc-Me), and of N_2 molecule, $\mu_N(N_2)$, respectively. The left plot in (a) shows the ΔE_f^{cub} curves for $Mo_{1-x}Ta_xN$, $Mo_{1-x}Ta_xN_{0.5}$, $(Mo_{1-x}Ta_x)_{0.875}N_{0.875}$, and $(Mo_{1-x}Ta_x)_{0.75}N$ for the nitrogen chemical potential of $\mu_N-\mu_N$ (N_2) = 0 eV and the right plot in (a) shows these ΔE_f^{cub} curves for $\mu_N - \mu_N(N_2) = -1.5$ eV. (b) Differences in energy of formation (ΔE_f) between hexagonal (E_f^{hex}), NiAs-type (empty hexagons) and WC-type (solid hexagons), and defect-free cubic (E_f^{cub}), NaCl-type structures. The defect-free situation is indicated by "no vacancies", while the further plots show the impact of 50% N-vacancies ("50% N vac"), 12.5% Schottky defects ("12.5% Schottky"), and 25% Me vacancies ("25% Me vac") on ΔE_f for these hexagonal structures ($\Delta E_f = E_f^{hex} - E_f^{cub}$ (defect-free)) but also for the cubic structure ($\Delta E_f = E_f^{cub} - E_f^{cub}$(defect-free)).
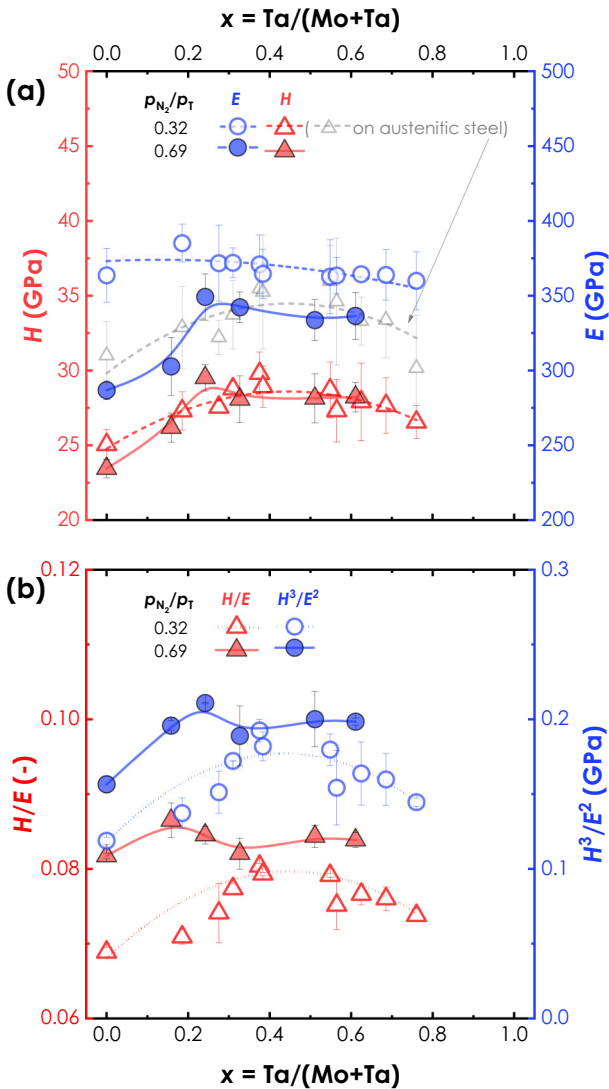
Fig. 7. (a) Indentation hardness (red) and modulus (blue) and (b) the ratios H/E and H^3/E^2 (red and blue, respectively) for the coatings on single-crystal (100) silicon wafers synthesised at low (empty symbols) and high (full symbols) nitrogen-to-total pressure ratios. Grey empty triangles in (a) indicate the indentation hardness of single-phase fcc-structured coatings (low p_{N2}/p_T ratio during deposition) grown on polycrystalline austenitic steel substrates.

3.2. Mechanical properties

As compared to γ-MoN$_{0.39}$ with its indentation hardness, H, of 25.0 ± 1.0 GPa, our quasi-binary cubic-structured coatings fcc-Mo$_{1-x}$Ta$_x$N$_y$ synthesised at low nitrogen-to-total pressure ratios show larger H values. Within the x range of 0.19–0.76, H varies between 27 and 30 GPa (with an average measurement accuracy of about 1.5 GPa), peaking for $x = 0.38$ ($H = 29.8 ± 1.4$ GPa) and hitting the bottom for $x = 0.76$ (26.6 ± 1.1 GPa), see Fig. 7a. The indentation modulus, E, remains nearly unchanged at around 360–370 GPa for the low N$_2$ containing sputter conditions. Consequently, the ratios H/E and H^3/E^2, which often serve as empirical criteria for the materials wear resistance, directly correlate with the hardness [55,56]. Accordingly, within the x range of 0.19–0.76, H/E and H^3/E^2 vary within 0.07–0.08 and 0.14–0.19 GPa, respectively, both peaking for $x = 0.38$, see Fig. 7b.

This is in contrast to the dual-phase coatings synthesised with the high nitrogen-to-total pressure ratio. Here, the indentation hardness and modulus behave similarly with increasing Ta content. Initially, with increasing Ta concentration x from 0 to 0.24, H increases from 23.4 ± 0.6 GPa to 29.5 ± 0.9 GPa and E increases from 287 ± 6 GPa to 349 ± 15 GPa, resulting in insignificant deviations of H/E from 0.08 and in a slight increase of H^3/E^2 from 0.16 GPa to 0.21 GPa. This correlates with an increasing fraction of the hexagonal phase (based on XRD, with the WC-type structure), compare with Fig. 6. With a further increase of Ta to 0.61, H and E remain within the error of measurement at about 28 GPa and 340 GPa (and consequently also H/E and H^3/E^2 at about of 0.08 and 0.2 GPa), respectively. In general, the dual-phase coatings synthesised with high p_{N2}/p_T show nearly the same hardness dependence on their Ta content as the single-phase fcc-structured ones synthesised with low p_{N2}/p_T. But their indentation modulus is lower especially for Ta contents below $x = 0.2$ (Fig. 7a). This leads to generally higher H/E and H^3/E^2 ratios (Fig. 7b).

Indentation hardness of the single-phase fcc-Mo$_{1-x}$Ta$_x$N$_y$ coatings correlates well with the residual stress, σ (empty blue circles in Fig. 8), as both properties increase by about 2 GPa with increasing Ta content up to $x \sim 0.6$. This stress dependence of the hardness values partly explains hardness enhancement of about 5 GPa for the coatings grown on austenitic steel substrates, where typically higher compressive residual stresses are accumulated than on Si substrates [57,58] – mainly because of the different coefficients of thermal expansion (CTE) between coating and substrates. While Si has typically a lower CTE than these nitride coatings, that of stainless steel is larger.

is preferred for Ta contents $x > 0.4$. If 25% Me vacancies form (i.e., solid solutions along the quasi-binary Mo$_{0.75}$N–Ta$_{0.75}$N tie line), the cubic NaCl-type is preferred for Ta contents $x > 0.2$, see the corresponding plots in Fig. 6b. Consequently, the composition range in which the cubic structure is preferred over the hexagonal one, can be tuned by the vacancy content. At the Mo-rich side, especially the N vacancies help, and at the Ta-rich side, especially the Me vacancies help.

The crystallisation of binary Ta–N coatings with two competing phases for low and high p_{N2}/p_T ratios suggests the formation of vacancy containing structures, because for vacancy-free structures, the hexagonal WC-type structure is clearly preferred. Especially the formation of 12.5% Schottky defected and 25% Me-vacant fcc-Ta–N is clearly preferred over their defected hexagonal WC-type counterparts, Fig. 6b. This is in agreement with the study of Pacher et al. [54] showing that ≥14% Me-vacant fcc-Ta–N are energetically more favourable than ≥14% Me-vacant hexagonal WC-type Ta–N and with the recent work of Abadias et al. [4] devoted to the vacancy-stabilised cubic tantalum nitride.
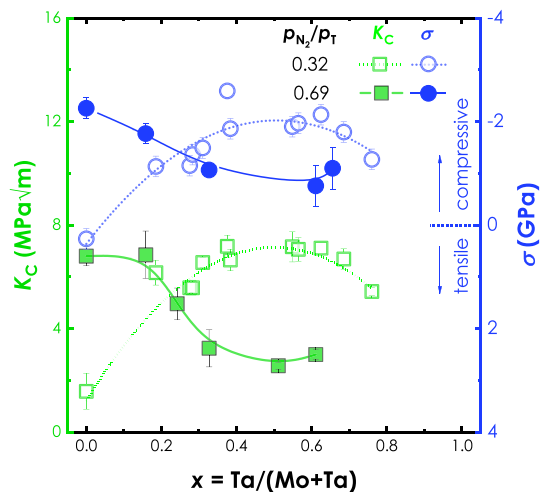

Fig. 8. (a) Apparent fracture toughness K_C (green square data points) and residual stresses σ (blue circle data points) of the coatings obtained at low (empty symbols) and high (full symbols) nitrogen-to-total pressure ratios, p_{N2}/p_T.
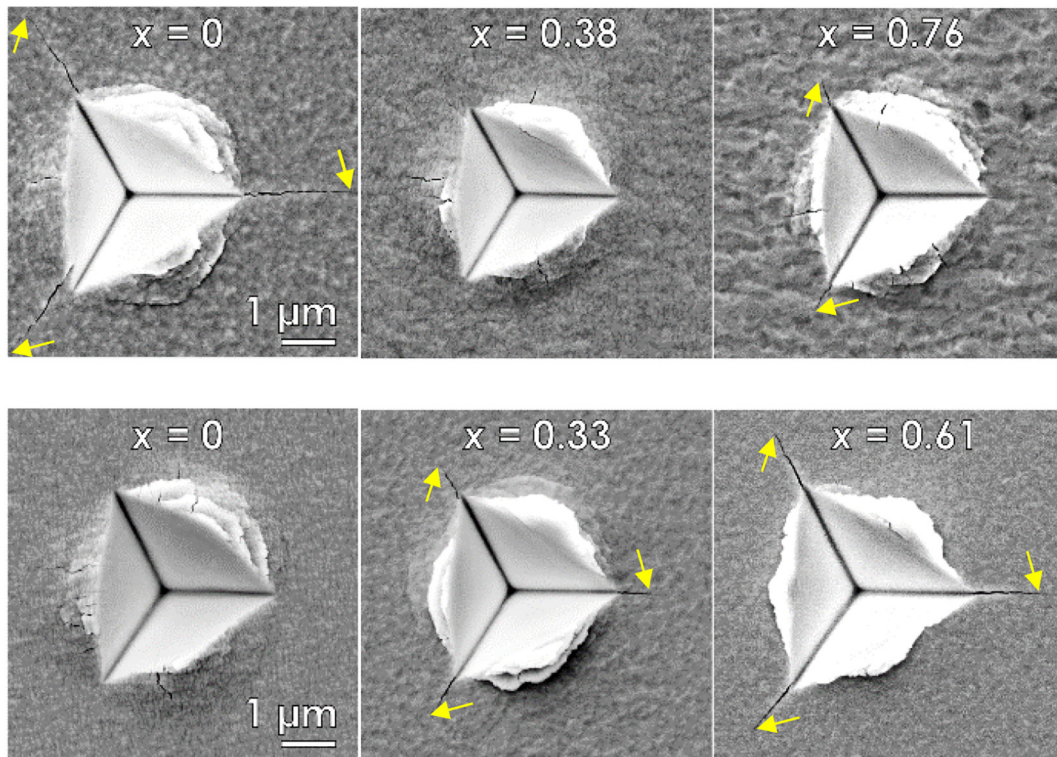
Fig. 9. SEM top-view images of the residual imprints after cube-corner nanoindentation with 150 mN on the Mo–Ta–N coatings synthesised at low (top raw) and high (bottom raw) p_{N2}/p_T ratios. Their corresponding Ta metal fraction Ta/(Mo + Ta), x, is given in the images. The yellow arrows indicate the crack tips.

Consequently, thermally induced tensile stresses are added to coatings on Si substrates, whereas thermally induced compressive stresses are added to coatings on austenitic steel substrates upon cooling to room temperature from the deposition temperature.

The residual stress furthermore excellently correlates with the apparent fracture toughness, K_C, of the single-phase fcc-Mo$_{1-x}$Ta$_x$N$_y$ (prepared at low nitrogen-to-total pressure ratio). With increasing Ta content from $x = 0$ to 0.38, σ changes gradually from +0.3 GPa (tensile residual stress) to −2.6 GPa (compressive residual stress), while K_C rises from 1.6 ± 0.7 MPa√m for γ-MoN$_{0.39}$ to 7.2 ± 0.4 MPa√m for Mo$_{0.62}$Ta$_{0.38}$N$_{0.52}$, see Fig. 8. Here, both properties reach a plateau for Ta contents up to $x = 0.69$, while further increasing x to 0.76 results in the relaxation of σ to −1.3 GPa and smaller K_C values of 5.4 ± 0.2 MPa√m.

It is worth emphasising again that such high K_C values aren't indicative of the intrinsic fracture toughness of the material system as they are strongly influenced by the residual stresses of type I. In fact, compressive residual stresses are an extrinsic toughening mechanism impeding crack growth by counteracting the stresses and strains experienced at the crack tip [59,60]. Resulting from the superposition of extrinsic and intrinsic effects, apparent fracture toughness should rather serve as a *qualitative* characteristic of the fracture behaviour of the system coating/substrate [61]. More sophisticated techniques are required to determine materials fracture toughness [62–64]. For example, a microcantilever bending test on free-standing coatings [65,66] yields lower values for transition-metal nitride coatings (below 5 and 3 MPa√m for TiN- and CrN-based compounds, respectively, as summarised by Glechner et al. [67]). However, even these values are influenced by residual stresses of type II and III.

For the coatings prepared with high p_{N2}/p_T, the apparent fracture toughness and residual stress have a slightly weaker correlation, probably due to their dual-phase nature. The highest K_C values of 6.8 ± 0.4 and 6.9 ± 0.9 MPa√m are observed for the partially ordered γ'-MoN$_{0.82}$ and the dual-phase ternary Mo$_{1-x}$Ta$_x$N$_y$ with the highest

fraction of a hexagonal phase ($x = 0.16$). These coatings also crystallised with the highest compressive stresses σ of about −2.3 and − 1.8 GPa, respectively. A lower fraction of a hexagonal phase at higher Ta contents results in much lower K_C and lower negative σ values (with the exception of the coating with $x = 0.24$). For Ta contents $0.33 <$ Ta/(Mo + Ta) < 0.66, the values of the apparent fracture toughness and compressive residual stress vary in the range 2.6–3.2 MPa√m and between −0.8 and − 1.1 GPa, respectively, nearly within the error of measurement. Even though these coatings crystallised mostly as fcc-Mo$_{1-x}$Ta$_x$N$_y$ (as revealed by XRD, Fig. 4), they exhibit a significantly lower apparent fracture toughness than those prepared at low p_{N2}/p_T.

The dependence of the apparent fracture toughness on the Ta content for both coating series, i.e. prepared with low and high p_{N2}/p_T, is also visible in the corresponding SEM top-view images of the imprints after the cube-corner nanoindentation tests, see Fig. 9. Clearly, the ternary single-phase fcc-Mo$_{1-x}$Ta$_x$N$_y$ coatings (upper row) with $x = 0.38$ and 0.76 as well as the γ'-MoN$_{0.82}$ (bottom row) exhibit the shortest cracks emanating from the imprint corners. A comparison with the SEM fracture cross-sections, Fig. 2, shows that this behaviour is not driven by their different growth morphology. In fact, a comparably high load of 150 mN turns out to be even below the cracking threshold of fcc-Mo$_{0.62}$Ta$_{0.38}$N$_{0.52}$ and γ'-MoN$_{0.82}$ coatings attesting to their exceptional crack resistance. Extruded material observed around the edges of the imprints of all coatings with high K_C values appears by virtue of an extensive plastic deformation and is typical for ductile materials.

4. Discussion

The presence of vacancies on either sublattice of Mo$_{1-x}$Ta$_x$N favours the formation of the fcc phase over the thermodynamically stable NiAs- (Mo-rich) or WC-type (Ta-rich) structures. While we were able to prepare single-phase fcc-Mo$_{1-x}$Ta$_x$N by using low p_{N2}/p_T during deposition, a competing hexagonal phase always formed at high p_{N2}/p_T. The best results in stabilising the fcc phase at high p_{N2}/p_T were achieved

within $0.33 < x < 0.66$, where the coatings contain only a small fraction of a hexagonal phase (hereafter we refer to these coatings as predominantly fcc-$Mo_{1-x}Ta_xN_y$). This in turn enables us to provide insights into the role of vacancy configuration and preferential orientation in mechanical performance of fcc-$Mo_{1-x}Ta_xN_y$.

Accordingly, high p_{N2}/p_T resulted in predominantly fcc-$Mo_{1-x}Ta_xN_y$ forming with a high concentration of vacancies on both sublattices, while low p_{N2}/p_T resulted in single-phase fcc-$Mo_{1-x}Ta_xN_y$ forming mainly with vacancies on the N sublattice, see Figs. 1, 5, and 6. This might have influenced the preferential orientation being (200) and (220) when using high p_{N2}/p_T and strongly (200) when using low p_{N2}/p_T during deposition, see Fig. 4. Cubic solid solutions stabilised by vacancies on both sublattices show a considerably lower (2.4 times lower on average) apparent fracture toughness than those stabilised by vacancies mainly on the nitrogen sublattice, but also exhibit only about a half of the compressive residual stress level. In absolute values, predominantly fcc-$Mo_{1-x}Ta_xN_y$ coatings stabilised by vacancies on both sublattices show comparably low K_C and σ values of about 2.9 MPa√m and −1.0 GPa, respectively. On the contrary, single-phase fcc-$Mo_{1-x}Ta_xN_y$ coatings stabilised by vacancies on the nitrogen sublattice exhibit K_C and σ values of about 7.0 MPa√m and −2 GPa, respectively. Nevertheless, their hardness values are in the range 28–30 GPa, showing differences only within the error of measurement.

In order to ascertain the causes of hardening and toughening, we shift our focus towards single-phase fcc-$Mo_{1-x}Ta_xN_y$ coatings, i.e. those prepared with low p_{N2}/p_T, which combine high fracture toughness with high hardness. The impact of residual stresses on apparent fracture toughness and indentation hardness of these fcc-$Mo_{1-x}Ta_xN_y$ coatings is highlighted again by showing the dependence of K_C and H on σ, Fig. 10. Both mechanical properties (K_C and H) exhibit nearly the same dependence on σ with the slopes dK_C/dσ and dH/dσ being −1.3 ± 0.5 MPa√m/GPa and −1.4 ± 0.3 GPa/GPa, respectively. An extrapolation to $\sigma = 0$ yields $K_C = 3.9 ± 0.5$ MPa√m – a plausible value for a ceramic material [68,69] – and H of 25.8 ± 0.8 GPa. It is noteworthy that similar values of indentation toughness can be obtained when K_C is corrected for the stress intensity factor given by Eq. (2) (see Table 1 in Supplementary Material). Thus, fcc-$Mo_{1-x}Ta_xN_y$ coatings appear to substantially outperform unalloyed γ-$MoN_{0.39}$ coatings with $K_C = 1.6 ± 0.7$ MPa√m in terms of indentation fracture toughness.

These results clearly reveal an extrinsic component of hardening and toughening of the single-phase cubic-structured coatings. Direct relationship between hardness or fracture toughness and residual stress in CVD and PVD coatings has been known for decades [70], and the growth of residual compressive stresses is often accompanied by increased indentation hardness [71–73] and toughness [61,74,75]. Residual stresses arise mainly due to the mismatch of the coefficients of thermal expansion between coating and substrate as well as from the growth process itself. Our calculations (not shown here) suggest that compositional variations along the $MoN_{0.5}$–TaN tie line do not notably affect thermal expansion coefficients of the solid solutions $Mo_{1-x}Ta_xN_{0.5(1+x)}$. Thus, the differences in the residual stresses are expected to arise mainly from the internal, growth-related stresses, which are cumulated by microstructural and chemical defects [76–81]. Such defects might form, for instance, during atomic peening of the growing coating with energetic Ar neutrals backscattered from the heavy target atoms [82–84]. The concentration of Ar in the coating is approximately proportional to $(M_i/M_{Ar})^2$, with M_i and M_{Ar} being the atomic masses of the target element and Ar, respectively [83,85]. Thus the higher the content of heavier Ta atoms in the target, the higher the content of Ar in particular and density of defects in general, which raise compressive residual stresses in the coating. (The fraction of Ar incorporated into the coatings deposited at high p_{N2}/p_T decreases due to a higher scattering probability of Ar neutrals in the gas phase and hence their thermalisation [82]. In the dual-phase coatings deposited at high p_{N2}/p_T, also the presence of a second phase with a different molar volume has to be taken into account.) A saturation or even an onset of compressive stress relaxation
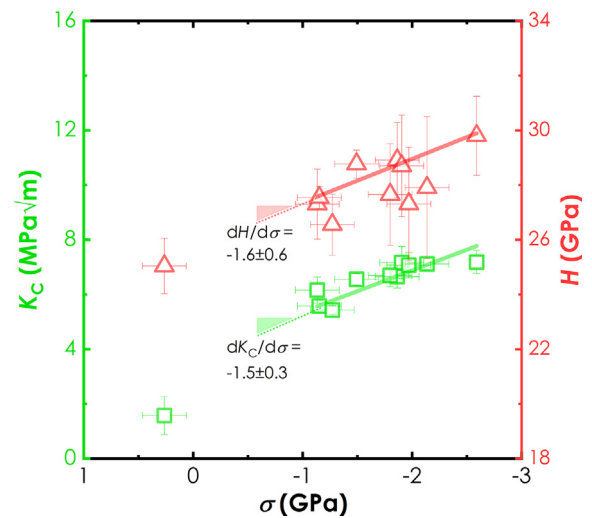

Fig. 10. Apparent fracture toughness, K_C, (green square data points) and indentation hardness, H, (red triangle data points) of the single-phase cubic-structured Mo–Ta–N coatings, prepared with $p_{N2}/p_T = 0.32$, as a function of their macroscopic residual stresses. The "isolated" data points at $\sigma = 0.3$ GPa are from the binary γ-$MoN_{0.39}$ coating prepared with $p_{N2}/p_T = 0.32$.

observed for higher concentration of Ta might be a result of other mechanisms coming into play such as, e.g., increasing homologous temperature/decreasing mobility of the adatoms (i.e. towards type I behaviour according to Abermann [86]) or decreasing deposition rate and consequently defect concentration [87,88]. (The latter also holds for the ternary coatings deposited at high p_{N2}/p_T, i.e. at lower deposition rates, showing lower compressive residual stresses).

It is noteworthy that we observe no correlation between residual stress and coating thickness, which exceeds 3 μm for nearly all single-phase fcc-$Mo_{1-x}Ta_xN_y$ (similar observations for the coatings thicker than 2 μm and deposited on Si (100) substrate were made by, e.g., Köstenbauer et al. [89] and Seidl et al. [58]). This might be due to the similar size of the grains and hence similar area density of the grain boundaries (GBs), which significantly influence intrinsic stresses [90–93]. Similar area density of GBs implies similar chemical potential gradient between surface and GBs – a driving force for weakly bounded interface/surface adatoms to migrate to the low-density disordered GBs [90] – and hence equal contribution to compressive residual stresses.

These considerations reveal, at least partly, the observed hardening and toughening of fcc-$Mo_{1-x}Ta_xN_y$ coatings. Larger compressive residual stresses are associated with higher density of defects acting as barriers to dislocation motion, thus increasing hardness, and higher compressive forces counteracting the stresses and strains experienced at the crack tip, thus impeding crack growth and increasing toughness. Also GBs strongly affect the mechanical response in general and fracture behaviour in particular of the fcc-$Mo_{1-x}Ta_xN_y$ coatings. Due to much lower fracture energy of GBs as compared to the grain interior, the crack propagates preferably along GBs [94,95]. For a columnar microstructure this implies a crack path leading through the entire thickness of the protective coating. Hence, along with the stress engineering, design of GBs, e.g. by twisting and tilting [96–99], activating delamination toughening [100] or influencing column boundaries by multilayer and superlattices [101,102], is vital to delay premature failure of such brittle coatings.

Another hardening and toughening mechanism might originate from the electronic structure, which can be substantially altered through alloying elements and vacancy content and configuration. Strengthening is naturally promoted by the bond energy (besides the microstructural obstacles impeding dislocation motion), determining the ease in nucleation and motion of dislocations. Holleck observed that the microhardness of non-stoichiometric transition-metal carbonitrides peaks in the vicinity of the valence electron concentration
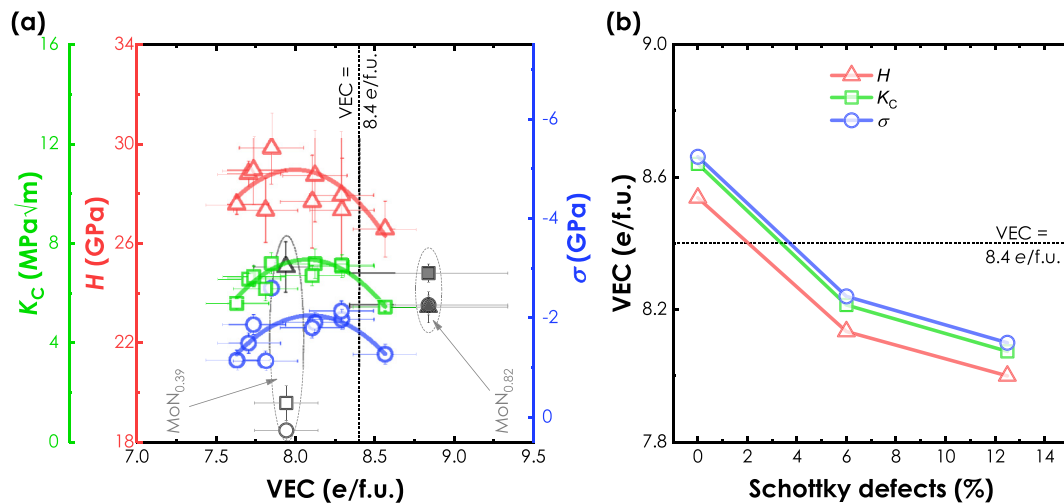
Fig. 11. (a) Indentation hardness, H, (red triangle points), apparent fracture toughness, K_c, (green square data points) and macroscopic residual stress, σ, (blue circle data points) of our single-phase fcc-structured $Mo_{1-x}Ta_xN_y$ coatings as a function of their valence electron concentration per unit cell. The data for single-phase cubic binary Mo–N coatings are added for comparison (empty symbols for low p_{N2}/p_T, solid symbols for high p_{N2}/p_T). The large error bars for VEC of γ-MoN$_{0.82}$ arise from the uncertainty in the metal vacancy concentration. (b) VEC position of the peaks in parabolic fits for H–VEC, K_C–VEC, and σ–VEC dependences using different concentrations of Schottky defect.

(VEC) of about 8.4 e/f.u. [103]. By approaching the VEC of 8.4–8.6 e/f.u., as shown by Jhi et al. [16], the shear-resistive p–d bonding states become fully occupied, resulting thus in the maximum of C_{44} [9,16]. The elastic shear stiffness C_{44} is in turn directly associated with the electronic response of the crystal to the applied shear strain and serves as a strong indicator of the bond energy. The ductility enhancement in transition-metal nitrides (reflected for instance by Pugh's [104] and Pettifor's [105] ductility criteria), was proposed by Sangiovanni et al. to originate from their electronic structure [22,106]. Accordingly, enhanced ductility is based on an increased volume fraction of metallic d–d bonding states, which is also reflected in higher VEC values. Highly populated metallic d–d bonding states allow in turn – as recently elucidated by Sangiovanni et al. with comprehensive molecular dynamics simulations [106] – the formation of new chemical bonds and absorb much higher stresses. The correlation of C_{44} and ductility criteria with the VEC was soon spread to many other non-stoichiometric compounds crystallising with the NaCl-type structure. Just recently Balasubramanian and co-workers extended this model in their computational research to many binary and ternary carbides, nitrides, and carbonitrides of transition metals of groups 4 to 12 [107].

In our earlier work, we observed hardening in γ-MoN$_x$ (with varying concentration of nitrogen vacancies) by approaching the VEC of 8.4–8.6 e/f.u. [19]. Both Mo–N and Ta–N are predicted to improve materials ductility [22]; although ductility is a necessary-but-not-sufficient condition for improved toughness, also enhanced fracture toughness was observed experimentally for nitride coatings when alloyed with Mo [2,108] or Ta [109]. The toughening effect for $V_{0.5}Mo_{0.5}N_x$ coatings, comprehensively investigated by Kindlund et al. [2,108,110], is based on the presence of nitrogen vacancies and the thereby associated increased volume fraction of metallic d–d bonding states, which allow the formation of new chemical bonds and hence absorb much higher stresses [106].

In order to calculate the VEC accurately, the structure and especially the vacancy concentration on either sublattice is of crucial importance. An indirect approach, requiring the knowledge of the composition, lattice constant, and atomic area density was recently suggested by Ozsdolay to distinguish between cation and anion vacancies [111,112]. In this work, we estimate the concentration of vacancies based on the elemental composition and by comparing experimental and computational stress-free lattice parameters and formation energies, that is in accord with the structural development along the MoN$_{0.5}$–Ta$_{0.875}$N$_{0.875}$ tie line. For such solid solutions (i.e., Mo$_{1-x}$Ta$_{0.875x}$N$_{0.5}$

$_{+0.375x}$), we observe the maxima of indentation hardness, apparent fracture toughness, and residual stresses (actually the maxima of the parabolic fits) in the vicinity of VEC = 8.0–8.1 e/f.u., see Fig. 11a. However, we need to mention that especially the concentration of Schottky defects (which are not easy to determine exactly) strongly influences this peak position as shown in Fig. 11b, which was not precisely determined in this work. Even most accurate chemical characterization such as ERDA or RBS will not provide information about the Schottky defect concentration. Therefore, we used chemical and structural investigations in combination with the density functional theory, to have at least a plausible estimation.

5. Summary and conclusions

Based on our experimental and ab initio results we conclude that single-phase cubic-structured coatings within the system Mo–Ta–N can be stabilised by tuning their vacancy configuration. Vacancies on the nitrogen sublattice (realised by a rather low nitrogen-to-total pressure ratio p_{N2}/p_T of 0.32 during reactive magnetron sputtering) guarantee for single-phase cubic-structured solid solutions up to a high Ta metal fraction, Ta/(Mo + Ta), of $x = 0.76$. Based on chemistry, lattice parameter variation, and energy of formation considerations, their fcc-Mo–Ta–N solid solutions basically follow the quasi-binary MoN$_{0.5}$–Ta$_{0.875}$N$_{0.875}$ tie line. Starting with a nearly 50% vacant N-sublattice in fcc-MoN$_{0.5}$, especially these vacancy sites are occupied (with N) upon increasing the Ta content x to 0.38, leading to continuously growing compressive residual stresses, hardness and apparent fracture toughness to −2.6 GPa, 30 GPa, and 7.2 MPa√m, respectively. Here, σ, H, and K_C reach their plateaus, showing deviations within the error of measurement for Ta contents up to $x = 0.69$. With higher Ta contents, a significant amount of metal vacancies will form, as the formation of Ta$_{0.875}$N$_{0.875}$ compounds (12.5% Schottky defects) is realistic based on chemistry, lattice parameter, and energy of formation considerations. Thereby, the compressive residual stresses, hardness, and apparent fracture toughness decrease to −1.3 GPa, 27 GPa, and 5.4 MPa√m, respectively, at $x = 0.76$.

Preparing the coatings with a significantly higher p_{N2}/p_T of 0.69 only allows for a single-phase fcc-structured coating when $x = 0$, hence, γ'-MoN$_{0.82}$. This binary forms with partially ordered vacancies and exhibits one of the highest compressive residual stresses of −2.3 GPa, apparent fracture toughness of 6.8 MPa√m, but also the lowest hardness of 23 GPa among all coatings tested. With increasing Ta content to

$x = 0.33$, soon a significant fraction of metal vacancies is formed favouring the fcc phase and leading to a drop in the apparent fracture toughness to 3.2 MPa√m and compressive residual stresses to −1.1 GPa, although the hardness increases to 28 GPa. Within the Ta-content range $0.33 < x < 0.66$, coatings contain only a small fraction of a hexagonal phase, while higher Ta contents promote the formation of the hexagonal phase.

The relatively small fraction of a hexagonal phase for coatings prepared with high p_{N2}/p_T if their Ta-fraction x is between 0.33 and 0.66, allows us to draw a comparison with the single-phase fcc-$Mo_{1-x}Ta_xN_y$ coatings prepared using low p_{N2}/p_T with a fair degree of accuracy. In other words, it allows to compare solid solutions stabilised by vacancies either on both sublattices or N sublattice. Accordingly, cubic solid solutions stabilised by vacancies mainly on the nitrogen sublattice clearly outperform those stabilised by vacancies on both sublattices, especially in terms of the apparent fracture toughness, by 140% on average. At the same time, however, they also show higher compressive residual stresses but a similar hardness.

Both hardness and apparent fracture toughness were found to correlate with residual stresses, which in turn are mainly controlled by the energetic vapour flux during the coating growth. The simultaneously good correlation with the VEC suggests that especially the hardening effect in single-phase fcc-$Mo_{1-x}Ta_xN_y$ coatings could also originate from changes in the electronic structure, by populating the shear-resistive p–d bonding states.

The combination of experimental and theoretical studies allowed us to provide deep insights into the role of microstructure and defects in phase stability as well as hardening and toughening effects in the system Mo–Ta–N. Our results demonstrate the power of defects (especially point defects) in stabilising desired crystal structures (here fcc) and improving mechanical properties (hardness in combination with apparent fracture toughness) through the thereby tuned atomic (and possibly even electronic) configuration.

Data availability

Original data are available upon request from the authors.

Declaration of Competing Interest

None.

Acknowledgement

Credit author statement

Fedor F. Klimashin: Conceptualisation, Methodology, Validation, Formal analysis, Investigation, Data Curation, Writing - Original Draft, Writing - Review & Editing, Visualisation, Project administration. **Lorenz Lobmaier:** Validation, Formal analysis, Investigation, Data Curation Writing - Review & Editing. **Nikola Koutná:** Validation, Formal analysis, Investigation, Data Curation, Writing - Review & Editing. **David Holec:** Conceptualisation, Methodology, Writing - Review & Editing. **Paul H. Mayrhofer:** Conceptualisation, Methodology, Resources, Writing - Review & Editing, Supervision, Funding acquisition.

Declaration of Competing Interest

The authors declare that they have no known competing financial interests or personal relationships that could have appeared to influence the work reported in this paper.

Appendix A. Supplementary data

Supplementary data to this article can be found online at https://doi.org/10.1016/j.matdes.2021.109568.

References

[1] L. Toth, Transition Metal Carbides and Nitrides, Academic Press, 1971.

[2] H. Kindlund, D. Sangiovanni, J. Lu, J. Jensen, V. Chirita, J. Birch, I. Petrov, J. Greene, L. Hultman, Vacancy-induced toughening in hard single-crystal V 0.5 Mo 0.5 Nx/MgO (001) thin films, Acta Mater. 77 (2014) 394–400, https://doi.org/10.1016/j.actamat.2014.06.025.

[3] F.F. Klimashin, H. Euchner, P.H. Mayrhofer, Computational and experimental studies on structure and mechanical properties of Mo-Al-N, Acta Mater. 107 (2016) 273–278, https://doi.org/10.1016/j.actamat.2016.01.063.

[4] G. Abadias, C.H. Li, L. Belliard, Q.M. Hu, N. Greneche, P. Djemia, Large influence of vacancies on the elastic constants of cubic epitaxial tantalum nitride layers grown by reactive magnetron sputtering, Acta Mater. 184 (2020) 254–266, https://doi.org/10.1016/j.actamat.2019.11.041.

[5] A.B. Mei, H. Kindlund, E. Broitman, L. Hultman, I. Petrov, J.E. Greene, D.G. Sangiovanni, Adaptive hard and tough mechanical response in single-crystal B1 VNx ceramics via control of anion vacancies, Acta Mater. 192 (2020) 78–88, https://doi.org/10.1016/j.actamat.2020.03.037.

[6] H. Euchner, P. Mayrhofer, H. Riedl, F. Klimashin, A. Limbeck, P. Polcik, S. Kolozsvari, Solid solution hardening of vacancy stabilized Ti x W 1− x B 2, Acta Mater. 101 (2015) 55–61, https://doi.org/10.1016/j.actamat.2015.08.048.

[7] V. Moraes, C. Fuger, V. Paneta, D. Primetzhofer, P. Polcik, H. Bolvardi, M. Arndt, H. Riedl, P. Mayrhofer, Substoichiometry and tantalum dependent thermal stability of α-structured W-Ta-B thin films, Scr. Mater. 155 (2018) 5–10, https://doi.org/10.1016/j.scriptamat.2018.06.005.

[8] R. Hahn, V. Moraes, A. Limbeck, P. Polcik, P.H. Mayrhofer, H. Euchner, Electron-configuration stabilized (W, Al) B2 solid solutions, Acta Mater. 174 (2019) 398–405, https://doi.org/10.1016/j.actamat.2019.05.056.

[9] S.H. Jhi, S.G. Louie, M.L. Cohen, J. Ihm, Vacancy hardening and softening in transition metal carbides and nitrides, Phys. Rev. Lett. 86 (15) (2001) 3348–3351, https://doi.org/10.1103/PhysRevLett.86.3348.

[10] J. Emmerlich, D. Music, P. Eklund, O. Wilhelmsson, U. Jansson, J.M. Schneider, H. Högberg, L. Hultman, Thermal stability of Ti 3 SiC 2 thin films, Acta Mater. 55 (4) (2007) 1479–1488, https://doi.org/10.1016/j.actamat.2006.10.010.

[11] M. Baben, L. Shang, J. Emmerlich, J.M. Schneider, Oxygen incorporation in M2AlC (M= Ti, V, Cr), Acta Mater. 60 (12) (2012) 4810–4818, https://doi.org/10.1016/j.actamat.2012.05.011.

[12] H. Riedl, T. Glechner, T. Wojcik, N. Koutná, S. Kolozsvári, V. Paneta, D. Holec, D. Primetzhofer, P. Mayrhofer, Influence of carbon deficiency on phase formation and thermal stability of super-hard TaCy thin films, Scr. Mater. 149 (2018) 150–154, https://doi.org/10.1016/j.scriptamat.2018.02.030.

[13] R. Hollerweger, D. Holec, J. Paulitsch, M. Bartosik, R. Daniel, R. Rachbauer, P. Polcik, J. Keckes, C. Krywka, H. Euchner, P.H. Mayrhofer, Complementary ab initio and X-ray nanodiffraction studies of Ta2O5, Acta Mater. 83 (2015) 276–284, https://doi.org/10.1016/j.actamat.2014.10.006.

[14] E.D. Hanson, L. Lajaunie, S.Q. Hao, B.D. Myers, F.Y. Shi, A.A. Murthy, C. Wolverton, R. Arenal, V.P. Dravid, Systematic study of oxygen vacancy tunable transport properties of few-layer MoO3-x enabled by vapor-based synthesis, Adv. Funct. Mater. 27 (17) (2017) 1605380, https://doi.org/10.1002/adfm.201605380.

[15] D.R. Islamov, V.A. Gritsenko, T.V. Perevalov, V.A. Pustovarov, O.M. Orlov, A.G. Chernikova, A.M. Markeev, S. Slesazeck, U. Schroeder, T. Mikolajick, G.Y. Krasnikov, Identification of the nature of traps involved in the field cycling of Hf0.5Zr0.5O2-based ferroelectric thin films, Acta Mater. 166 (2019) 47–55, https://doi.org/10.1016/j.actamat.2018.12.008.

[16] S.H. Jhi, J. Ihm, S.G. Louie, M.L. Cohen, Electronic mechanism of hardness enhancement in transition-metal carbonitrides, Nature 399 (6732) (1999) 132–134, https://doi.org/10.1038/20148.

[17] T. Glechner, P.H. Mayrhofer, D. Holec, S. Fritze, E. Lewin, V. Paneta, D. Primetzhofer, S. Kolozsvari, H. Riedl, Tuning structure and mechanical properties of Ta-C coatings by N-alloying and vacancy population, Sci. Rep. 8 (1) (2018) 17669, https://doi.org/10.1038/s41598-018-35870-x.

[18] J.S.K.L. Gibson, S. Rezaei, H. Ruess, M. Hans, D. Music, S. Wulfinghoff, J.M. Schneider, S. Reese, S. Korte-Kerzel, From quantum to continuum mechanics: studying the fracture toughness of transition metal nitrides and oxynitrides, Materials Research Letters 6 (2) (2018) 142–151, https://doi.org/10.1080/21663831.2017.1414081.

[19] F.F. Klimashin, N. Koutna, H. Euchner, D. Holec, P.H. Mayrhofer, The impact of nitrogen content and vacancies on structure and mechanical properties of Mo-N thin films, J. Appl. Phys. 120 (18) (2016) 185301, https://doi.org/10.1063/1.4966664.

[20] N. Koutna, D. Holec, O. Svoboda, F.F. Klimashin, P.H. Mayrhofer, Point defects stabilise cubic Mo-N and Ta-N, J. Phys. D. Appl. Phys. 49 (37) (2016) 375303, https://doi.org/10.1088/0022-3727/49/37/375303.

[21] K. Balasubramanian, S.V. Khare, D. Gall, Energetics of point defects in rocksalt structure transition metal nitrides: thermodynamic reasons for deviations from stoichiometry, Acta Mater. 159 (2018) 77–88, https://doi.org/10.1016/j.actamat.2018.07.074.

[22] D.G. Sangiovanni, L. Hultman, V. Chirita, Supertoughening in B1 transition metal nitride alloys by increased valence electron concentration, Acta Mater. 59 (5) (2011) 2121–2134, https://doi.org/10.1016/j.actamat.2010.12.013.

[23] G. Greczynski, S. Mraz, L. Hultman, J.M. Schneider, Venting temperature determines surface chemistry of magnetron sputtered TiN films, Appl. Phys. Lett. 108 (4) (2016)https://doi.org/10.1063/1.4940974 041603.

[24] D. Rafaja, C. Wustefeld, C. Baehtz, V. Klemm, M. Dopita, M. Motylenko, C. Michotte, M. Kathrein, Effect of Internal Interfaces on Hardness and Thermal Stability of Nanocrystalline Ti0.5Al0.5N Coatings, Metallurgical and Materials Transactions a-Physical Metallurgy and Materials Science, 42a(3), 2011 559–569, https://doi.org/10.1007/s11661-010-0204-8.

[25] N. Koutna, D. Holec, M. Friak, P.H. Mayrhofer, M. Sob, Stability and elasticity of metastable solid solutions and superlattices in the MoN-TaN system: first-principles calculations, Mater. Des. 144 (2018) 310–322, https://doi.org/10.1016/j.matdes.2018.02.033.

[26] A.C. Fischer-Cripps, Nanoindentation, Springer, 2011.

[27] F.F. Klimashin, P.H. Mayrhofer, Ab initio-guided development of super-hard Mo–Al–Cr–N coatings, Scr. Mater. 140 (2017) 27–30, https://doi.org/10.1016/j.scriptamat.2017.06.052.

[28] W.C. Oliver, G.M. Pharr, An improved technique for determining hardness and elastic modulus using load and displacement sensing indentation experiments, J. Mater. Res. 7 (6) (1992) 1564–1583, https://doi.org/10.1557/Jmr.1992.1564.

[29] A.C. Fischer-Cripps, Critical review of analysis and interpretation of nanoindentation test data, Surf. Coat. Technol. 200 (14–15) (2006) 4153–4165, https://doi.org/10.1016/j.surfcoat.2005.03.018.

[30] F.F. Klimashin, H. Riedl, D. Primetzhofer, J. Paulitsch, P.H. Mayrhofer, Composition driven phase evolution and mechanical properties of Mo–Cr–N hard coatings, J. Appl. Phys. 118 (2) (2015), 025305, https://doi.org/10.1063/1.4926734.

[31] B. Lawn, R. Wilshaw, Indentation fracture: principles and applications, J. Mater. Sci. 10 (6) (1975) 1049–1081, https://doi.org/10.1007/Bf00823224.

[32] A.G. Evans, E.A. Charles, Fracture toughness determinations by indentation, J. Am. Ceram. Soc. 59 (7–8) (1976) 371–372, https://doi.org/10.1111/j.1151-2916.1976.tb10991.x.

[33] B.R. Lawn, A.G. Evans, D.B. Marshall, Elastic/plastic indentation damage in ceramics: the median/radial crack system, J. Am. Ceram. Soc. 63 (9–10) (1980) 574–581, https://doi.org/10.1111/j.1151-2916.1980.tb10768.x.

[34] G. Anstis, P. Chantikul, B.R. Lawn, D. Marshall, A critical evaluation of indentation techniques for measuring fracture toughness: I, direct crack measurements, J. Am. Ceram. Soc. 64 (9) (1981) 533–538, https://doi.org/10.1111/j.1151-2916.1981.tb10320.x.

[35] D. Harding, W. Oliver, G. Pharr, Cracking during nanoindentation and its use in the measurement of fracture toughness, MRS Online Proceedings Library Archive 356 (1994) 663–668, https://doi.org/10.1557/PROC-356-663.

[36] G. Pharr, D. Harding, W. Oliver, Measurement of fracture toughness in thin films and small volumes using nanoindentation methods, Mechanical Properties and Deformation Behavior of Materials Having Ultra-Fine Microstructures, Springer 1993, pp. 449–461.

[37] G. Pharr, Measurement of mechanical properties by ultra-low load indentation, Mater. Sci. Eng. A 253 (1–2) (1998) 151–159, https://doi.org/10.1016/S0921-5093(98)00724-2.

[38] T.W. Scharf, H. Deng, J.A. Barnard, Mechanical and fracture toughness studies of amorphous SiC-N hard coatings using nanoindentation, J. Vac. Sci. Technol. A 15 (3) (1997) 963–967, https://doi.org/10.1116/1.580788.

[39] J.J. Kibler, R. Roberts, The effect of biaxial stresses on fatigue and fracture, J. Manuf. Sci. Eng. 92 (4) (1970) 727–734, https://doi.org/10.1115/1.3427838.

[40] D.B. Marshall, R.F. Cook, N.P. Padture, M.L. Oyen, A. Pajares, J.E. Bradby, I.E. Reimanis, R. Tandon, T.F. Page, G.M. Pharr, B.R. Lawn, The compelling case for indentation as a functional exploratory and characterization tool, J. Am. Ceram. Soc. 98 (9) (2015) 2671–2680, https://doi.org/10.1111/jace.13729.

[41] K. Bobzin, High-performance coatings for cutting tools, CIRP J. Manuf. Sci. Technol. 18 (2017) 1–9, https://doi.org/10.1016/j.cirpj.2016.11.004.

[42] G.G. Stoney, The tension of metallic films deposited by electrolysis, Proceedings of the Royal Society of London. Series A, Containing Papers of a Mathematical and Physical Character 82 (553) (1909) 172–175, https://doi.org/10.1098/rspa.1909.0021.

[43] W.D. Nix, Mechanical properties of thin films, Metall. Trans. A. 20 (11) (1989) 2217–2245, https://doi.org/10.1007/Bf02666659.

[44] G.C.A.M. Janssen, M.M. Abdalla, F. van Keulen, B.R. Pujada, B. van Venrooy, Celebrating the 100th anniversary of the Stoney equation for film stress: developments from polycrystalline steel strips to single crystal silicon wafers, Thin Solid Films 517 (6) (2009) 1858–1867, https://doi.org/10.1016/j.tsf.2008.07.014.

[45] D. Marshall, B.R. Lawn, Residual stress effects in sharp contact cracking, J. Mater. Sci. 14 (8) (1979) 2001–2012, https://doi.org/10.1007/Bf00551043.

[46] G. Kresse, J. Furthmuller, Efficient iterative schemes for ab initio total-energy calculations using a plane-wave basis set, Phys. Rev. B Condens. Matter 54 (16) (1996) 11169–11186, https://doi.org/10.1103/physrevb.54.11169.

[47] G. Kresse, J. Hafner, Ab initio molecular dynamics for liquid metals, Phys. Rev. B Condens. Matter 47 (1) (1993) 558–561, https://doi.org/10.1103/physrevb.47.558.

[48] J.P. Perdew, K. Burke, M. Ernzerhof, Generalized gradient approximation made simple, Phys. Rev. Lett. 77 (18) (1996) 3865, https://doi.org/10.1103/PhysRevLett.77.3865.

[49] S. Wei, L.G. Ferreira, J.E. Bernard, A. Zunger, Electronic properties of random alloys: special quasirandom structures, Phys. Rev. B Condens. Matter 42 (15) (1990) 9622–9649, https://doi.org/10.1103/physrevb.42.9622.

[50] C. Stampfl, A. Freeman, Metallic to insulating nature of TaN x: role of Ta and N vacancies, Phys. Rev. B 67 (6) (2003), 064108, https://doi.org/10.1103/PhysRevB.67.064108.

[51] L. Pankratz, Thermodynamic Properties of Carbides, Nitrides, and Other Selected Substances, 1994.

[52] G.L.W. Hart, B.M. Klein, Phonon and elastic instabilities in MoC and MoN, Phys. Rev. B 61 (5) (2000) 3151–3154, https://doi.org/10.1103/PhysRevB.61.3151.

[53] K. Bouamama, P. Djemia, M. Benhamida, First-principles calculation of the structural and elastic properties of ternary metal nitrides TaxMo1-xN and TaxW1-xN, J. Phys. Conf. Ser. 640 (1) (2015), 012022, https://doi.org/10.1088/1742-6596/640/1/012022.

[54] F. Pacher, P.H. Mayrhofer, D. Holec, Vacancy-driven extended stability of cubic metastable Ta-Al-N and Nb-Al-N phases, Surf. Coat. Technol. 326 (2017) 37–44, https://doi.org/10.1016/j.surfcoat.2017.07.012.

[55] A. Leyland, A. Matthews, On the significance of the H/E ratio in wear control: a nanocomposite coating approach to optimised tribological behaviour, Wear 246 (1–2) (2000) 1–11, https://doi.org/10.1016/S0043-1648(00)00488-9.

[56] X.Z. Ding, X.T. Zeng, Y.C. Liu, Structure and properties of CrAlSiN nanocomposite coatings deposited by lateral rotating cathod arc, Thin Solid Films 519 (6) (2011) 1894–1900, https://doi.org/10.1016/j.tsf.2010.10.022.

[57] G. Kleer, R. Kassner, E.-M. Meyer, M. Schinker, W. Doell, Effect of process parameters on the residual stresses and the wear behavior of aluminum nitride physical vapor deposition coatings, Metallurgical Coatings and Thin Films (1992) 167–172 Elsevier1992.

[58] W.M. Seidl, M. Bartosik, S. Kolozsvari, H. Bolvardi, P.H. Mayrhofer, Influence of coating thickness and substrate on stresses and mechanical properties of (Ti,Al,Ta)N/(Al,Cr)N multilayers, Surf. Coat. Technol. 347 (2018) 92–98, https://doi.org/10.1016/j.surfcoat.2018.04.060.

[59] R.O. Ritchie, The conflicts between strength and toughness, Nat. Mater. 10 (11) (2011) 817–822, https://doi.org/10.1038/Nmat3115.

[60] R.O. Ritchie, Mechanisms of fatigue crack-propagation in metals, Ceramics and Composites - Role of Crack Tip Shielding, Mat Sci Eng a-Struct 103 (1) (1988) 15–28, https://doi.org/10.1016/0025-5416(88)90547-2.

[61] R. Soler, S. Gleich, C. Kirchlechner, C. Scheu, J.M. Schneider, G. Dehm, Fracture toughness of Mo2BC thin films: intrinsic toughness versus system toughening, Mater. Des. 154 (2018) 20–27, https://doi.org/10.1016/j.matdes.2018.05.015.

[62] M. Sebastiani, K.E. Johanns, E.G. Herbert, G.M. Pharr, Measurement of fracture toughness by nanoindentation methods: recent advances and future challenges, Curr Opin Solid St M 19 (6) (2015) 324–333, https://doi.org/10.1016/j.cossms.2015.04.003.

[63] G. Dehm, B.N. Jaya, R. Raghavan, C. Kirchlechner, Overview on micro- and nanomechanical testing: new insights in interface plasticity and fracture at small length scales, Acta Mater. 142 (2018) 248–282, https://doi.org/10.1016/j.actamat.2017.06.019.

[64] J. Ast, M. Ghidelli, K. Durst, M. Goken, M. Sebastiani, A.M. Korsunsky, A review of experimental approaches to fracture toughness evaluation at the micro-scale, Mater. Des. 173 (2019) 107762, https://doi.org/10.1016/j.matdes.2019.107762.

[65] A. Riedl, R. Daniel, M. Stefenelli, T. Schoberl, O. Kolednik, C. Mitterer, J. Keckes, A novel approach for determining fracture toughness of hard coatings on the micrometer scale, Scr. Mater. 67 (7–8) (2012) 708–711, https://doi.org/10.1016/j.scriptamat.2012.06.034.

[66] D. Di Maio, S. Roberts, Measuring fracture toughness of coatings using focused-ion-beam-machined microbeams, J. Mater. Res. 20 (2) (2005) 299–302, https://doi.org/10.1557/JMR.2005.0048.

[67] T. Glechner, R. Hahn, T. Wojcik, D. Holec, S. Kolozsvári, H. Zaid, S. Kodambaka, P. Mayrhofer, H. Riedl, Assessment of ductile character in superhard Ta-CN thin films, Acta Mater. 179 (2019) 17–25, https://doi.org/10.1016/j.actamat.2019.08.015.

[68] A.G. Evans, Perspective on the development of high-toughness ceramics, J. Am. Ceram. Soc. 73 (2) (1990) 187–206, https://doi.org/10.1111/j.1151-2916.1990.tb06493.x.

[69] B. Lawn, Fracture of Brittle Solids, Cambridge university press, 1993.

[70] D.T. Quinto, Mechanical property and structure relationships in hard coatings for cutting tools, J. Vac. Sci. Technol. A 6 (3) (1988) 2149–2157, https://doi.org/10.1116/1.575206.

[71] L. Karlsson, A. Hörling, M. Johansson, L. Hultman, G. Ramanath, The influence of thermal annealing on residual stresses and mechanical properties of arc-evaporated TiCxN1− x (x= 0, 0.15 and 0.45) thin films, Acta Mater. 50 (20) (2002) 5103–5114, https://doi.org/10.1016/S1359-6454(02)00365-8.

[72] Z.-H. Xu, X. Li, Influence of equi-biaxial residual stress on unloading behaviour of nanoindentation, Acta Mater. 53 (7) (2005) 1913–1919, https://doi.org/10.1016/j.actamat.2005.01.002.

[73] N. Huber, J. Heerens, On the effect of a general residual stress state on indentation and hardness testing, Acta Mater. 56 (20) (2008) 6205–6213, https://doi.org/10.1016/j.actamat.2008.08.029.

[74] L.Q. Zhang, H.S. Yang, X.L. Pang, K.W. Gao, A.A. Volinsky, Microstructure, residual stress, and fracture of sputtered TiN films, Surf. Coat. Technol. 224 (2013) 120–125, https://doi.org/10.1016/j.surfcoat.2013.03.009.

[75] S. Zhang, Thin Films and Coatings: Toughening and Toughness Characterization, CRC Press, 2015.

[76] R. Hoffman, The mechanical properties of thin condensed films, in: G. Hass, R. Thun (Eds.), Physics of Thin Films, Academic Press, New York, 1966.

[77] M.F. Doerner, W.D. Nix, Stresses and deformation processes in thin films on substrates, Critical Reviews in Solid State and Materials Sciences 14 (3) (1988) 225–268, https://doi.org/10.1080/10408438808243734.

[78] H. Oettel, R. Wiedemann, S. Preissler, Residual stresses in nitride hard coatings prepared by magnetron sputtering and arc evaporation, Surf. Coat. Technol. 74 (1995) 273–278, https://doi.org/10.1016/0257-8972(95)08235-2.

[79] G.C.A.M. Janssen, Stress and strain in polycrystalline thin films, Thin Solid Films 515 (17) (2007) 6654–6664, https://doi.org/10.1016/j.tsf.2007.03.007.

[80] E. Chason, P.R. Guduru, Tutorial: understanding residual stress in polycrystalline thin films through real-time measurements and physical models, J. Appl. Phys. 119 (19) (2016) 191101, https://doi.org/10.1063/1.4949263.

[81] G. Abadias, E. Chason, J. Keckes, M. Sebastiani, G.B. Thompson, E. Barthel, G.L. Doll, C.E. Murray, C.H. Stoessel, L. Martinu, Review article: stress in thin films and coatings: current status, challenges, and prospects, J. Vac. Sci. Technol. A 36 (2) (2018), 020801, https://doi.org/10.1116/1.5011790.

[82] H.F. Winters, E. Kay, Gas incorporation into sputtered films, J. Appl. Phys. 38 (10) (1967) 3928–3934, https://doi.org/10.1063/1.1709043.

[83] J.A. Thornton, J. Tabock, D.W. Hoffman, Internal stresses in metallic films deposited by cylindrical magnetron sputtering, Thin Solid Films 64 (1) (1979) 111–119, https://doi.org/10.1016/0040-6090(79)90550-9.

[84] A. Pan, J.E. Greene, Residual compressive stress in sputter-deposited TiC films on steel substrates, Thin Solid Films 78 (1) (1981) 25–34, https://doi.org/10.1016/0040-6090(81)90414-4.

[85] H. Windischmann, Intrinsic stress in sputter-deposited thin films, Crit Rev Solid State 17 (6) (1992) 547–596, https://doi.org/10.1080/10408439208244586.

[86] R. Abermann, Measurements of the intrinsic stress in thin metal films, Vacuum 41 (4–6) (1990) 1279–1282, https://doi.org/10.1016/0042-207X(90)93933-A.

[87] A. Fillon, G. Abadias, A. Michel, C. Jaouen, Stress and microstructure evolution during growth of magnetron-sputtered low-mobility metal films: influence of the nucleation conditions, Thin Solid Films 519 (5) (2010) 1655–1661, https://doi.org/10.1016/j.tsf.2010.07.091.

[88] E. Chason, M. Karlson, J.J. Colin, D. Magnfalt, K. Sarakinos, G. Abadias, A kinetic model for stress generation in thin films grown from energetic vapor fluxes, J. Appl. Phys. 119 (14) (2016) 145307, https://doi.org/10.1063/1.4946039.

[89] H. Köstenbauer, G.A. Fontalvo, M. Kapp, J. Keckes, C. Mitterer, Annealing of intrinsic stresses in sputtered TiN films: the role of thickness-dependent gradients of point defect density, Surf. Coat. Technol. 201 (8) (2007) 4777–4780, https://doi.org/10.1016/j.surfcoat.2006.10.017.

[90] E. Chason, B.W. Sheldon, L.B. Freund, J.A. Floro, S.J. Hearne, Origin of compressive residual stress in polycrystalline thin films, Phys. Rev. Lett. 88 (15) (2002) 156103, https://doi.org/10.1103/PhysRevLett.88.156103.

[91] R. Daniel, K.J. Martinschitz, J. Keckes, C. Mitterer, The origin of stresses in magnetron-sputtered thin films with zone T structures, Acta Mater. 58 (7) (2010) 2621–2633, https://doi.org/10.1016/j.actamat.2009.12.048.

[92] R. Daniel, D. Holec, M. Bartosik, J. Keckes, C. Mitterer, Size effect of thermal expansion and thermal/intrinsic stresses in nanostructured thin films: experiment and model, Acta Mater. 59 (17) (2011) 6631–6645, https://doi.org/10.1016/j.actamat.2011.07.018.

[93] R. Daniel, J. Keckes, I. Matko, M. Burghammer, C. Mitterer, Origins of microstructure and stress gradients in nanocrystalline thin films: the role of growth parameters and self-organization, Acta Mater. 61 (16) (2013) 6255–6266, https://doi.org/10.1016/j.actamat.2013.07.009.

[94] G.T. Hahn, The influence of microstructure on brittle fracture toughness, Metall. Trans. A. 15 (6) (1984) 947–959, https://doi.org/10.1007/Bf02644685.

[95] S.M. Wiederhorn, Brittle fracture and toughening mechanisms in ceramics, Annu. Rev. Mater. Sci. 14 (1) (1984) 373–403, https://doi.org/10.1146/annurev.ms.14.080184.002105.

[96] M. Gell, E. Smith, The propagation of cracks through grain boundaries in polycrystalline 3% silicon-iron, Acta Metall. 15 (2) (1967) 253–258, https://doi.org/10.1016/0001-6160(67)90200-3.

[97] T. Watanabe, S. Tsurekawa, Toughening of brittle materials by grain boundary engineering, Mat Sci Eng a-Struct 387 (2004) 447–455, https://doi.org/10.1016/j.msea.2004.01.140.

[98] R. Daniel, M. Meindlhumer, W. Baumegger, J. Zalesak, B. Sartory, M. Burghammer, C. Mitterer, J. Keckes, Grain boundary design of thin films: using tilted brittle interfaces for multiple crack deflection toughening, Acta Mater. 122 (2017) 130–137, https://doi.org/10.1016/j.actamat.2016.09.027.

[99] R. Daniel, M. Meindlhumer, W. Baumegger, J. Todt, J. Zalesak, T. Ziegelwanger, C. Mitterer, J. Keckes, Anisotropy of fracture toughness in nanostructured ceramics controlled by grain boundary design, Mater. Des. 161 (2019) 80–85, https://doi.org/10.1016/j.matdes.2018.11.028.

[100] L. Liu, Q. Yu, Z. Wang, J. Ell, M. Huang, R.O. Ritchie, Making ultrastrong steel tough by grain-boundary delamination, Science (2020)https://doi.org/10.1126/science.aba9413.

[101] M. Schlogl, C. Kirchlechner, J. Paulitsch, J. Keckes, P.H. Mayrhofer, Effects of structure and interfaces on fracture toughness of CrN/AlN multilayer coatings, Scr. Mater. 68 (12) (2013) 917–920, https://doi.org/10.1016/j.scriptamat.2013.01.039.

[102] R. Hahn, M. Bartosik, R. Soler, C. Kirchlechner, G. Dehm, P.H. Mayrhofer, Superlattice effect for enhanced fracture toughness of hard coatings, Scr. Mater. 124 (2016) 67–70, https://doi.org/10.1016/j.scriptamat.2016.06.030.

[103] H. Holleck, Material selection for hard coatings, J. Vac. Sci. Technol. A 4 (6) (1986) 2661–2669, https://doi.org/10.1116/1.573700.

[104] S. Pugh, XCII. Relations between the elastic moduli and the plastic properties of polycrystalline pure metals, The London, Edinburgh, and Dublin Philosophical Magazine and Journal of Science, 45(367), 1954 823–843, https://doi.org/10.1080/14786440808520496.

[105] D.G. Pettifor, Theoretical predictions of structure and related properties of Intermetallics, Mater. Sci. Technol. 8 (4) (1992) 345–349, https://doi.org/10.1179/mst.1992.8.4.345.

[106] D.G. Sangiovanni, Inherent toughness and fracture mechanisms of refractory transition-metal nitrides via density-functional molecular dynamics, Acta Mater. 151 (2018) 11–20, https://doi.org/10.1016/j.actamat.2018.03.038.

[107] K. Balasubramanian, S.V. Khare, D. Gall, Valence electron concentration as an indicator for mechanical properties in rocksalt structure nitrides, carbides and carbonitrides, Acta Mater. 152 (2018) 175–185, https://doi.org/10.1016/j.actamat.2018.04.033.

[108] H. Kindlund, G. Greczynski, E. Broitman, L. Martinez-de-Olcoz, J. Lu, J. Jensen, I. Petrov, J.E. Greene, J. Birch, L. Hultman, V0.5Mo0.5Nx/MgO(001): Composition, nanostructure, and mechanical properties as a function of film growth temperature, Acta Mater. 126 (2017) 194–201, https://doi.org/10.1016/j.actamat.2016.12.048.

[109] W.M. Seidl, M. Bartosik, S. Kolozsvari, H. Bolvardi, P.H. Mayrhofer, Influence of Ta on the fracture toughness of arc evaporated Ti-Al-N, Vacuum 150 (2018) 24–28, https://doi.org/10.1016/j.vacuum.2018.01.028.

[110] H. Kindlund, D.G. Sangiovanni, I. Petrov, J.E. Greene, L. Hultman, A review of the intrinsic ductility and toughness of hard transition-metal nitride alloy thin films, Thin Solid Films 688 (2019) 137479, https://doi.org/10.1016/j.tsf.2019.137479.

[111] B.D. Ozsdolay, C.P. Mulligan, K. Balasubramanian, L. Huang, S.V. Khare, D. Gall, Cubic β-WN layers: growth and properties vs N-to-W ratio, Surf. Coat. Technol. 304 (2016) 98–107, https://doi.org/10.1016/j.surfcoat.2016.06.079.

[112] B.D. Ozsdolay, K. Balasubramanian, D. Gall, Cation and anion vacancies in cubic molybdenum nitride, J. Alloys Compd. 705 (2017) 631–637, https://doi.org/10.1016/j.jallcom.2017.02.072.